Viral fusion proteins of classes II and III but not of class I sense the lipid composition of host membranes

Chetan S Poojari*, Tobias Bommer, Jochen S Hub*

Theoretical Physics and Center for Biophysics, Saarland University, Saarbrücken, Germany

*Correspondance to: chetan.poojari@uni-saarland.de; jochen.hub@uni-saarland.de

Viral infection requires stable binding of viral fusion proteins to host membranes, which contain hundreds of lipid species. How viruses sense lipid compositions to target suitable host cells is poorly understood. Using multi-scale molecular simulations, we computed 66 membrane binding free energies of fusion proteins from classes I–III with various lipid compositions and identified distinct mechanisms of lipid recognition. We find that membrane binding of class II and III proteins, but not of class I proteins, is greatly modulated by the content of polyunsaturated lipids, cholesterol, anionic lipids, or gangliosides. Fusion proteins bind specific membranes by chemically recognizing distinct head group moieties and by sensing packing defects. The results show that lipid recognition of class II and III fusion proteins is a key feature to selectively bind to mammalian plasma membranes or to membranes of the endosomal compartments.

Introduction

The transmission of emerging and re-emerging viruses from animals to humans is of major concern as outbreaks of viral diseases have ravaged humanity and have imposed economic burden worldwide. For the majority of viruses, no vaccines are available or they are only little effective due to adaptability of viruses (*1*). For the development of therapeutics against viral infections, understanding of host–pathogen interactions is vital. Many pathogenic viruses are enclosed by a lipid envelope that, upon infection, fuses either with the plasma membrane (PM) or with the endosomal membranes of the host cell (*2, 3*). Viruses make use of fusion proteins to overcome the energetic barriers along the fusion pathway (*4–10*). However, how viruses interact with the host membrane is not well understood.

Viral fusion proteins are grouped into three classes based on structural similarity (*1, 11*). Class I fusion proteins are typified by a trimeric alpha-helical coiled-coil structure in the postfusion state. The group encompasses fusion proteins of respiratory viruses such as influenza hemagglutinin (HA2) or the SARS-Cov-2 spike protein (*12*). Class II proteins are formed of beta-sheet rich domains and are found in arthropod-borne viruses such as Rift Valley fever virus (glycoprotein Gc), dengue virus or yellow fever virus, which causes hemorrhagic fevers (*13*). Class III protein structures adopt a combination of coiled-coil and beta-sheet domains and are found in viruses such as herpesviruses (glycoprotein gB) or vesicular stomatitis virus, which primarily affect swine, horses, and cattle (*14, 15*).

Despite structural differences, all viral fusion proteins undergo a structural rearrangement which is a prerequisite for membrane fusion. Specific trigger induces the conformational change in fusion proteins resulting in exposure of fusion peptides in class I proteins or fusion loops in class II and III proteins which bind to the host cell membrane anchoring

the fusogen (Fig. 1). Subsequently, the fusion protein contracts, thereby forcing the host and the viral membranes into spatial proximity. Hence, strong and selective protein–lipid binding is required to recognize the host cell membrane and to withstand the forces exerted on the membranes during the fusion process.

Several studies revealed that cholesterol plays an important role during membrane fusion (*13, 15–24*). For example, the fusion protein of Semliki Forest virus binds to the membrane only in the presence of cholesterol, where the fusion loops form direct contacts with cholesterol as shown by photo-cholesterol cross-linking experiments (*16*). A point mutation (A226V) rendered membrane binding by Chikungunya virus dependent on cholesterol (*25*). However, fusion proteins may also recognize phospholipids, as shown by the crystal structure of the Rift Valley fever virus (RVFV) Gc protein in complex with short-tailed phosphocholine lipid (*13*). Furthermore, glycosphingolipids have been associated with viral entry into host cells (*22, 26–28*). These studies highlight the important role of lipids during viral infection.

In this work, we combined coarse-grained and atomistic molecular dynamics (MD) simulations together with free energy calculations to quantify the binding of one representative of each fusion protein class to lipid membranes, namely class I influenza hemagglutinin (IAV HA2), class II Gc protein from RVFV, and class III gB protein from pseudorabies virus (PrV, Fig. 1). We computed binding affinities to complex plasma membrane models and to a large set of binary and ternary membrane models involving different head groups, tail lengths, tail unsaturations, and sterol content. The simulations reveal specific lipid binding sites, unspecific lipid association, as well as drastic effects of lipid composition and protein class on membrane binding. Our simulation results are supported by a large body of previous experimental data.

Results

Membrane binding affinities follow the order class I > class II $\gtrsim$ class III

To investigate the energetics of fusion peptide or loop insertion into a complex membrane, we set up coarse-grained simulations systems composed of a fusion protein and a plasma membrane (PM) model, with the lipid composition of a typical outer leaflet of a mammalian PM (Table S1). Based on a recent lipidomics study (*29*), the membrane was composed of 40% cholesterol, 25% phosphatidylcholine (PC), 25% sphingomyelin (SM), 4% glycosphingolipid (GM3), 4% phosphatidylserine (PS), and 2% phosphatidylethanolamine (PE, Table S1). We used umbrella sampling to compute the potential of mean force (PMF) of protein binding to the membrane. According to the PMFs, the binding affinity ΔG_{bind} to the PM is stronger (more negative) for IAV HA2 ($-115\,\text{kJ/mol}$) as compared to RVFV Gc ($-82\,\text{kJ/mol}$) and PrV gB ($-59\,\text{kJ/mol}$) (Fig. 2 D,E). The stronger membrane anchoring of IAV HA2 is rationalized by the insertion of a large hydrophobic fusion peptide into the hydrophobic core of the membrane, as opposed to RVFV Gc or PrV gB that anchor to the membrane by insertion of only two or one bulky aromatic side chains per monomer, respectively (Fig. 6, 7). In addition, fusion peptides of HA2 are connected to the central helix by flexible loops, which enable the fusion peptides to reorient and insert deep into the membrane, whereas the fusion loops are structurally constrained to the folded protein, thus allowing the insertion of only one or two aromatic side chains.

To determine whether the differences in binding affinities are specific to the simulated HA2, Gc, and gB, or whether they represent general trends among class I, II, and III fusion proteins, we carried out an extensive sequence analysis. We compared sequences of 23 fusion proteins from class I, 33 fusion proteins from class II, and 18 fusion proteins from class III (Fig. 3, Tables S5–S7). Remarkably, among many fusion proteins, the sequence

identities among fusion loops/peptides (Fig. 3, upper triangles) exceed by far the sequence identities among the complete fusion proteins (Fig. 3, lower triangles), demonstrating the functional importance of fusion loops/peptides for viral replication.

According to the sequence identity matrices, class I fusion proteins are highly diverse, exhibiting low sequence identity even within the same family. However, similar to IAV HA2, all class I fusion proteins contain several hydrophobic amino acids, thereby, enabling the insertion of fusion peptides into the host membrane with high affinity (Table S5). Class II fusion proteins are highly conserved within the families of hantaviridae, togaviridae and flaviviridae with sequence identities in the range of 40–60% (Fig. 3B, lower triangle), while the respective fusion loops reach sequence identities of more than 80% (Fig. 3B, upper triangle). In agreement with RVFV Gc, most of the class II fusion loops analyzed here contain one phenylalanine and one tryptophane that may insert into the membrane, although few exceptions exist for which tryptophane is replaced with a hydrophobic leucine or isoleucine residue (Table S6). Among class III, fusion proteins exhibit a low degree of conservation with an exception for the baculoviridae family. Notably, albeit low conservation between the complete fusion proteins of baculoviridae and some genera within orthomyxoviridae families, the matrix reveals high conservation between the fusion loops of these families, indicating their evolutionary relation (*30*) (Fig. 3C, central blocks). Depending on the class III family, the fusion loops contain mostly one hydrophobic aromatic residue (Phe/Trp) per monomer to insert into the membrane, although exceptions with up to three hydrophobic aromatic residues exist (Table S7).

Thus, the strong binding observed for IAV HA2 is expected for other class I fusion proteins, which likewise anchor to the host PM by the insertion of fusion peptides. Since many class II proteins insert two aromatic residues per monomer into the membrane, while most class III proteins insert only one aromatic residue per monomer, we expect

that the binding affinities to the PM typically follow Class I > Class II $\gtrsim$ Class III. Exceptions to this order exist (Tables S5–S7). Notably, despite the presence of only two or one aromatic sites in the fusion loops of RVFV Gc and PrV gB, we find remarkably strong affinities ΔG_{bind} of $-82\,\text{kJ/mol}$ or $-59\,\text{kJ/mol}$, respectively, suggesting that the affinity is also based on specific interactions with lipid headgroups and modulated by the degree of lipid unsaturation. Hence, we identified and quantified the effects of specific lipids on fusion protein binding.

Membrane binding affinity strongly depends on the lipid composition

By computing PMFs of binding for a large set of membranes, we found that ΔG_{bind} is strongly modulated by the lipid composition. Specifically, binding is enhanced by the presence of polyunsaturated lipids, cholesterol, gangliosides, and for class II and III proteins, by anionic lipids.

Polyunsaturated lipids bind to specific interaction sites

The outer leaflet of the PM is enriched with PC lipids with varying tail lengths and degrees of unsaturation. To clarify how lipid tails influence ΔG_{bind}, we computed PMFs for fusion protein binding to binary lipid membranes containing 40% cholesterol plus one type of PC lipid with varying tail properties. The PMFs reveal increased binding affinity (more negative ΔG_{bind}), upon replacing one of the saturated palmitic acid tails 16:0 of DPPC with the unsaturated oleic acid tail 18:1 of POPC. The effect is drastic for IAV HA2 for which ΔG_{bind} decreases from $-33\,\text{kJ/mol}$ to $-99\,\text{kJ/mol}$.

To validate our membrane affinity calculations and, thereby, the strong binding affinity of IAV HA2, we computed additional PMFs of insertion of a single IAV HA2 fusion peptide into membranes of POPC or POPC:POPG (80%:20%), for which experimental

binding data is available for comparison. Experiments revealed ΔG_{bind} of a single IAV HA2 fusion peptide of $-32.35\,\mathrm{kJ/mol}$ or $-31.8\,\mathrm{kJ/mol}$ for POPC or POPC:POPG membranes, respectively (*31*). In our simulations, ΔG_{bind} was $-33.3\,\mathrm{kJ/mol}$ or $-27.9\,\mathrm{kJ/mol}$ for POPC or POPC:POPG membranes, respectively, in good agreement with the experimental values, hence validating the simulation protocol (Fig. S1). Notably, the binding affinity of the trimer is not three times the affinity of the fusion peptide monomer, possibly because binding of the entire fusion protein involves a larger perturbation of the membrane as compared to binding of only the three fusion peptides (Fig. S1).

Next, we introduced lipids with increasing number of double bonds. Compared to POPC, the binding to DOPC with a double bond in each tail is greatly enhanced by 32 kJ/mol for IAV HA2, but only slightly enhanced for for RVFV Gc and PrV gB (Fig. 2D). Increasing the unsaturation of the PC lipid tail from oleic acid 18:1 (POPC) to linoleic acid 18:2 (PLPC) enhances the affinity moderately by 10 to 14 kJ/mol. Further increasing the tail length and unsaturation from linoleic acid 18:2 (PLPC) to arachidonic acid 20:4 (PAPC) induces increasingly stronger binding for all the three fusion proteins, with the largest effect on binding for IAV HA2 (Fig. 2D). These results demonstrate that binding of viral fusion proteins to membranes is largely enhanced with increasing tail unsaturation (*32, 33*).

As evident from binding affinities (Fig. 2D), IAV HA2 binds strongly to lipid membranes irrespective of the membrane composition, whereas the binding of RVFV Gc and PrV gB are sensitive to the lipid composition. To trace the specific lipids required for class II or class III binding, we analyzed the enrichment of lipids at the membrane/protein interface (Fig. 2B/C, S2–S5). The enrichment maps reveal binding sites at the RVFV Gc and PrV gB surfaces, which may be categorized into two types of interactions: (i) involving highly localized, specific interactions with binding pockets (Figs. 2B and S3, grey and

red circles) and (ii) wider distributed, more unspecific interactions at the protein surface (Fig. 2B, black arrows). The binding pocket of RVFV Gc (Fig. 2B, red circles) has been identified previously by crystallography (*13*), whereas the binding pocket of Gc marked with grey circles as well as the binding pocket of PrV gB (Fig. S3, circles) are, to our knowledge, reported for the first time. In contrast to class II and III proteins, the class I HA2 does not contain binding pockets as evident from the dispersed lipid enrichment maps (Fig. S1).

To test whether lateral lipid sorting promotes binding, in addition to specific binding sites, we analyzed the enrichment of lipids at the protein–membrane interface (Fig. 2C). We find that polyunsatuated lipids are strongly enriched at the protein irrespective of the type of lipid headgroup and protein class, highlighting the role of polyunsatuated lipids in membrane recognition. Hence, polyunsaturated lipids promote binding not only by increasing the average membrane disorder, but furthermore by the formation of localized highly disordered patches via lateral sorting.

Taken together, the membrane binding affinities of class I, II and III proteins strongly increase in presence of polyunsaturated lipids. Only in case of class II and III proteins, the lipids bind to well-defined binding pockets.

RVFV Gc and PrV gB are sensitive to cholesterol concentration, but not IAV HA2

With a molar concentration of approximately 40% (*29*), cholesterol is the most abundant lipid in the mammalian PM estimated, where it plays a functional role during viral infection as shown by previous experiments (*13, 15–24*). To rationalize cholesterol-dependent binding of viral proteins found in experiments (*13, 15*), we set up PMF calculations with DOPC as a reference lipid plus increasing cholesterol concentration of 0%, 20%, or 40%. Here, we chose DOPC as reference lipid because experimental binding data for RVFV Gc

and PrV gB are available for comparison (*13, 15*) .

In qualitative agreement with experiments, RVFV Gc and PrV gB bind to the membrane in a cholesterol-dependent manner (Fig. 4). In binding experiments, RVFV Gc binding to liposomes required at least 20% cholesterol, and binding increased with cholesterol concentration (*13*), in line with the trends in our simulations. For PrV gB, binding was reported at 40% cholesterol but not at 0% or 20% cholesterol concentration (*15*). These data are likewise in qualitative agreement with our simulations as we find generally weaker binding of gB as compared to Gc, rationalizing the increased requirement for cholesterol for obtaining stable binding. Although IAV HA2 binding increases with cholesterol content, HA2 binds to membrane with sufficient affinity of $-80\,\mathrm{kJ/mol}$ independent of cholesterol, in agreement with biochemical experiments showing influenza virus interactions with liposomes even in the absence of cholesterol (*34*).

Although the trends in binding affinities estimated from our simulations are in line with experimental findings, structural mechanisms by which cholesterol mediates viral protein–host membrane interactions are yet to be fully resolved. A previous study on RVFV Gc highlighted that cholesterol acts as a spacer between phospholipids to facilitate insertion of fusion loop residues into the hydrophobic membrane core; however, also direct cholesterol–fusion loop interactions were reported (*13*). Indeed, contact maps obtained from simulations of RVFV Gc and PrV gB revealed frequent interactions between cholesterol and fusion loop residues W821/F826 (RVFV Gc) or F275 (PrV gB) in all the binary and tertiary lipid membranes, with an exception of only rare interactions for PrV in DPPC membrane (Fig. S6, S7). Such direct interactions of cholesterol with fusion loop residues have also been observed by labeling with photocholesterol for Semliki Forest virus but could not be detected in case of dengue virus (*16*). Our simulations together with earlier studies rationalize the strict cholesterol requirement for binding of RVFV Gc and

PrV gB; namely, (i) cholesterol acts as a spacer between phospholipids, thereby allowing bulky aromatic fusion loop residues to penetrate the head group region during initial binding, while (ii) direct interactions between cholesterol and fusion loop bulky residues may further stabilize the protein–membrane interactions.

Viral proteins differ in their sensitivity to headgroups (PC, PE, PS, PI)

The outer leaflet of the PM contains small amounts of phospholipids with PE, PS and phosphatidylinositol (PI) headgroups, with relative molar concentration below 2% (*29*). To understand if any of the low-concentration lipids play a role in membrane binding, we systematically varied the headgroup among PC, PE, PS and PI (Fig. 2 D). We set up membranes containing 55% PLPC, 5% of a second phospholipid with varying headgroup but with the same acyl chain length and degree of unsaturation, as well as 40% cholesterol. PLPC was chosen as reference due to its high abundance in the outer leaflet of the PM (Table S2).

For IAV HA2, the overall strong binding affinity is only mildly modulated by the headgroup type (Fig. 2D). RVFV Gc and PrV gB do not distinguish between PC and PE headgroups as indicated by similar ΔG_{bind}, in line with experiments on gB (*15*). Regarding RVFV Gc, the observed similar binding for PC and PE lipids is in agreement with biolayer interferometry (BLI) experiments which showed that PE lipids restore RVFV Gc binding when added to liposomes composed of SM and cholesterol (*13*). Our atomistic simulations (see below) further corroborate the experimental findings, as we observe PE lipids to occupy the same binding site as PC lipids (Fig. S8). However, RVFV Gc reveals stronger binding to anionic headgroups (PS and PI), whereas PrV gB reveals stronger binding only to PI headgroups. Such increased affinity to anionic lipids are rationalized by additional electrostatic interactions of cationic residues near the lipid binding pockets.

Together, PE, PS, and PI lipids may enhance or recover fusion protein binding; these findings are significant since the viruses investigated in this study as well as several other viruses can fuse with endosomal membranes, which contain higher concentrations of PE, PS, and PI lipids as compared to the outer leaflet of the PM (*3, 35–40*). Indeed, the stronger binding of Gc to PS and PI headgroups, and PrV gB to PI headgroups correlates with the Gc/gB entry via the endocytic pathway (*35, 36*). Furthermore, the requirement of anionic PS for fusion has been shown for dengue and vesicular stomatitis viruses, which belong to class II and III, respectively (*41, 42*).

Previous experiments investigated the effect of a mutation in the lipid binding pocket of RVFV Gc on membrane binding (*13*). Mutating the choline-interacting aspartic acid D961 to lysine resulted in loss of binding to PC/cholesterol membranes owing to electrostatic repulsion between the cationic lysine and choline moieties; however, binding was rescued upon the addition of anionic PS lipids, which was attributed to favorable PS–lysine interactions (*13*). These data provided insight into the lipid specificity of class II fusion proteins and may further validate our binding affinity calculations. In line with the experiments, the Gc wild type binds membranes with and without PS lipids with similar affinity, indicating that PS lipids are insignificant for wild type binding (Fig. 5). In contrast, the D961K mutant binds to PS-containing membranes with 20 kJ/mol higher affinity as compared to PS-free membranes, corresponding to ∼3000-fold increased binding probability. Visual inspection of the simulations confirmed that the recovery of binding by the D961K mutant upon the addition of PS lipid was due to the formation of PS–lyine salt bridges (Fig. 2B, 6E). The lipid-sensitivity of residue 961 found in simulation and experiments confirms the importance of the PC binding site and further validates our simulation protocol.

Fully saturated sphingomyelin (SM) reduces binding, whereas unsaturated SM does not interfere with binding

Along with PC lipids, sphingomyelin (SM) is highly abundant phospholipid in the outer leaflet of the PM. Binding experiments have shown weak binding or complete loss of binding by RVFV Gc to liposomes containing palmitoyl sphingomyelin (PSM) or PSM/cholesterol, respectively (*13*). However, recent lipidomics data has shown that the outer leaflet of the PM contains a large fraction of SM with long or unsaturated chain fatty acids such as 18:1-24:0 or 18:1-24:1 (*29*).

To investigate how SM affects binding free energies, we set up systems with varying SM tail length and unsaturation (Fig. 2D). Addition of palmitoyl sphingomyelin (PSM, 18:1-16:0) to the reference lipid mixture of PLPC/cholesterol reduces the binding affinity (increases ΔG_{bind}) in line with experimental binding data (*13*). However, we found that weak binding is recovered upon increasing the tail length or unsaturation from C16:0 to C24:0 (LSM) or C24:1 (NSM). Similar effect are found for IAV HA2 binding. For PrV gB, in contrast, the SM tail length and unsaturation have only a minor effect on binding, in line with experiments showing that PrV gB binding strictly requires 40% cholesterol but does not depend on SM or other lipid content (*15*). We explain the observed difference in binding upon addition of SM species by the varied membrane-stiffening properties of SM species, which follow order of PSM (16:0) > LSM (24:0) > NSM (24:1) (*43,44*).

Atomistic models of RVFV Gc and PrV gB interactions with lipids

To validate the binding sites observed in coarse-grained simulations described above, and to obtain atomistic insight into lipid interactions with RVFV Gc and PrV gB, we backmapped equilibrated coarse-grained systems to atomistic resolution and carried

out all-atom MD simulations with a total simulation time of 40 μs. For resolution transformation, we selected systems with varying headgroups and tail lengths, such as POPC/cholesterol, PAPC/cholesterol, PLPC/PAPS/cholesterol, PLPC/PAPE/cholesterol, and PLPC/GM3/cholesterol. Figures 6 and 7 show snapshots after 2 μs of simulation for PAPC or PAPS binding to RVFV Gc as well as for PAPC or GM3 binding to PrV gB, respectively. Similar interactions were found for POPC or PAPE (Figs. S8–S9). RVFV Gc binds to the PAPC/cholesterol membrane via insertion of bulky fusion loop residues W821 and F826 into the hydrophobic membrane core, but also via interactions of interfacial rim residues R775, R776, H778, H784, N827, and N829 with the polar headgroups (Fig. 6C).

In addition to these unspecific interactions, the simulations identified lipid binding sites in agreement with crystallographic data and previous simulations (*13*) (Fig. 6B,D–E, S8; Fig. 2, red circles). For instance, the headgroup of PAPC fits deeply into the binding site where the choline and phosphate groups may form hydrogen bonds with the side chains of D271 and R776, respectively, while the polyunsaturated tail (20:4) packs against the membrane-inserted F826 side chain (Fig. 6D, S8). Notably, we observed that the same binding site may be occupied by PAPS because the serine amino and carboxyl groups of PS may form favorable hydrogen bonds with the backbone oxygen and side chain of R775, respectively (Fig. 6E). Other interactions of PAPS are similar to those observed with PAPC. This remarkable promiscuity of the RVFV Gc lipid binding site provides the structural rationale for nearly identical affinity of Gc to membranes containing PC or PS lipids (Fig. 5).

Figure 7A–D shows PrV gB binding to the PAPC/cholesterol membrane via insertion of the fusion loop residue F275 into the hydrophobic membrane core and by interactions of the interfacial rim residues Y192, W187 and Y276 with the polar head groups (Fig. 7C).

PAPC binds to a groove of PrV gB lined by fusion loops (FL) 1 and 2 of two different monomers (Fig. 7B/D. Fig. S3 and S5, red circles). Here, the choline headgroup binds deep into the pocket forming hydrogen bonds with residues D239 and Y276 (FL2, monomer 1) as well as cation-π interaction with W187 (FL1, monomer 1). PAPC binding is further stabilized by interactions of lipid phosphate oxygen atoms with the H277 side chain (FL2, monomer 2) and with the backbone nitrogen atom of T278 (FL2, monomer 2). In addition, a carbonyl oxygen of the lipid ester group engages in a hydrogen bond with Y276 (FL2, monomer 2). Similar to the binding found for RVFV Gc, the lipid tail packs against the membrane-inserted F275 side chain. As shown in Fig. 7E, the GM3 sugar headgroup may occupy the same binding site as PAPC where it interacts with residues lining FL1 and FL2 from two different monomers.

Our multi-microsecond time scale atomistic simulations validate the lipid binding sites identified from coarse-grained simulations. The simulations of RVFV Gc validate a crystallographic binding site for PC headgroup, while also showing PE and PS lipids binding to the same pocket (Figs. S8 and S9). In addition, MD simulations reveal a second binding site for RVFV Gc (Fig. 2B, S4 (gray circles) and S8C). For PrV gB, the simulations reveal a lipid binding site between fusion loops of two different monomers, characterized by a different binding mode as compared to class II proteins. The second lipid binding site of RVFV Gc and the binding site of PrV gB found here are yet to be experimentally confirmed.

Gangliosides acts as co-receptors for viral protein attachment to host cells

The outer leaflet of the PM contains lipids with sugar headgroups (gangliosides) with a total concentrations below 5% (*29*), which have previously been shown to play a role during

viral infection (*22, 27, 28*). To reveal how the ganglioside GM3 affects membrane binding of viral fusion proteins, we compared binding free energies obtained in absence or presence of GM3. Upon removal of GM3, binding affinities were reduced by ∼15–30 kJ/mol across the investigated fusion proteins, quantifying the role of GM3 as co-receptor (Fig 2D). To structurally explain the effect of GM3 on protein binding, we assessed the lateral density and enrichment of GM3 around the proteins (Fig 2B,C, Figs. S2–S5). These data reveal broad density distributions of GM3 at the protein surface, indicative of unspecific yet favorable binding. In addition, for PrV gB, GM3 is enriched at the lipid binding site, which is also accessible to PC, PE, or PS lipids (Fig. S3, red circles).

To validate the GM3 binding site, we backmapped a PrV gB-PLPC/cholesterol/GM3 coarse-grained system (structure at 15 μs) to all-atom resolution. Within a follow-up two-microsecond atomistic simulation, and in agreement with the CG models, GM3 continued to associate with the lipid binding site (Fig. 7E). The binding and enrichment of gangliosides to PrV gB observed in our simulations are in line with experiments that imaged PrV co-localization with another gangliosides GM1 (*22*). For IAV HA2, the observed enrichment of GM3 lipids is compatible with experiments showing GM3 to act as a receptor for IAV HA2 binding and entry (*27, 28*). Similarly, we observe nonspecific binding of GM3 to RVFV Gc, which is yet to be confirmed experimentally; however, co-localiztion of dengue viruses to GM1 gangliosides has been reported recently, which also contains class II fusion proteins (*26*). Thus, while previous experiments revealed the role of gangliosides during viral infection (*22, 26–28*), we here provided the atomistic and energetic rationale for the action of ganglioside as co-receptor.

Discussion

Interactions of viral fusion proteins with the host PM are of high physiological relevance for two reasons: (i) selective lipid interactions enable the sensing of target host cells; (ii) membrane binding with high affinity is required to withstand forces during the fusion process. While there is extensive experimental data on fusion protein structures and some data on membrane composition-dependent binding of viral fusion proteins (*13, 15–24, 26–28, 45*), it is still experimentally challenging to obtain mechanistic insight into the binding of viral fusion proteins to host membranes. In this study, we computed the free energy of membrane binding for viral fusion proteins from class I, II, III to reveal how the lipid composition and protein properties regulate the binding affinity. We provided structural insight into the mechanism of lateral lipid sorting by viral fusion proteins, and we characterized the lipid binding sites on viral fusion proteins at atomistic resolution. The excellent agreement with a wide body of experimental data validates our simulation protocols for studying viral fusion protein–membrane interactions.

The PMFs show that class I:IAV HA2 binds to all simulated membranes with stronger affinity (ΔG_{bind} more negative) than class II:RVFV Gc or class III:PrV gB. Sequence conservation analysis across 74 fusion proteins from 13 viral families focusing on fusion peptides/loops indicates that the observed binding affinities are representative for many of the viral fusion proteins and follow class I > class II $\gtrsim$ class III (Fig. 3, Table S5–S7).

The IAV HA2 trimer binds to the plasma membrane with $\Delta G_{\text{bind}} = -115\,\text{kJ/mol}$ (Fig. 2 D,E), which has implications on the protein-mediated membrane fusion. Along the membrane fusion pathway, the first structural rearrangement is the formation of a stalk-like fusion intermediate. Aeffner *et al.* estimated the free–energy required to form a stalk-like structure in the absence of proteins in the range between ∼250 kJ/mol and ∼500

kJ/mol depending on the lipid composition (*8*). Hence, considering that the single IAV HA2 trimer binds with $-115\,\mathrm{kJ/mol}$, binding of at least three trimers to the host plasma membrane would provide the affinity to withstand the forces involved in stabilizing the stalk-like fusion intermediate, consistent with the experimental findings showing that at least three trimers are required to mediate fusion (*46–48*).

Unlike class I, the membrane binding affinities of class II or III viral proteins are highly regulated by membrane lipid composition and by the localization of specific lipid types at binding pockets of RVFV Gc and PrV gB (Fig. 2B/C, S2–S5). These results suggest that class I and class II/III fusion proteins utilize different mechanisms of binding to host membranes. In case of class I, mere insertion of fusion peptides followed by folding of the protein is sufficient to pull the two opposing membrane together, whereas, class II/III viral proteins, in addition to insertion of fusion loops, also require binding of specific lipids at binding pockets to withstand large forces during membrane fusion. Notably, we observe that the binding affinity of RVFV Gc and PrV gB may be enhanced or recovered by anionic PS or PI lipids, which correlates with the endocytic pathway taken by these viruses, hence involving the fusion with membranes enriched with anionic lipids (*35, 36*).

The viral protein–lipid interactions not only depends on the lipid headgroup type, but also strongly on the degree of unsaturation of the lipid tails. PMFs show that binding affinities increase with increasing number of double bonds in the lipid tails (Fig. 2D). The effect of lipid tail unsaturation on binding affinity is rationalized by the high flexibility of polyunsaturated acyl chains, enabling the lipids to adapt to the membrane perturbations imposed by fusion protein binding. Namely, the insertion of fusion peptide/loops into the membrane creates voids underneath the protein, while polyunsaturated lipids are well suited to fit their headgroups into the binding pockets and, simultaneously, fill the voids beneath the protein with their flexible acyl chains. Such dual function would not

be possible by lipids carrying saturated or shorter tails. In addition to the above functions, Pinot *et al.* showed that polyunsaturated lipids (C18:0 - C22:6) are also capable of inducing shallow defects in the membrane (*32*), which may be filled with the fusion peptides/loops upon membrane binding, thereby further increasing binding affinity. The multi–functionality of polyunsaturated lipids, along with the ability of the viral fusion proteins to discriminate lipid tails, gives viral fusion proteins a significant advantage to carry out their functions. The enrichment of polyunsaturated lipids around viral proteins is significant in the light of our recent study on stalk formation, where we showed that the free energy required to form a stalk-like fusion intermediate is greatly reduced in presence of polyunsaturated lipids (*49*). Thus, the protein-bound polyunsaturated lipids may serve as a platform to stabilize the stalk-like fusion intermediate. Taken together, our simulations reveal the important role of polyunsaturated lipids during various stages of virus infection. Our results rationalize recent findings from Farley *et al.* (*33*), who showed that SARS-CoV-2 reprograms host lipid synthesis to increase the abundance of PC lipids with polyunsaturated tails.

Previous experimental results (*13, 15–24*) and our simulation show that cholesterol serves a dual role during fusion protein binding. Namely, cholesterol creates voids between lipid head groups by acting as a spacer, resembling the formation of shallow defects by polyunsaturated lipids (*32*). In addition, cholesterol forms direct interactions with fusion loops (*13, 16*). The combination of cholesterol and polyunsaturated lipids greatly favor host membrane targeting by viral fusion proteins.

Lastly, we provided energetic and molecular rationale for the role of gangliosides as co-receptor during viral entry into host cells (*22, 26–28*). We find non-specific broad distributions of the ganglioside GM3 around viral proteins, indicating that sugar headgroups of ganglioside may serve as a initial attachment for viral proteins prior to binding to the

membrane surface. The findings are important for our understanding of viral entry since membrane protein receptors have not been identified for all viral proteins (*26*). Notably, the role of gangliosides as co-receptor for virus attachment to host cells are reminiscent of their role during membrane targeting by bacterial toxins such as shiga toxin (*50*) and cholera toxin (*51*).

Overall, we revealed molecular mechanisms and energetics by which viral fusion proteins from classes I, II, and III bind to host plasma membranes with complex lipid composition. We found that membrane binding by class II and III proteins greatly depends on lipid composition, thus enabling viruses to sense specific membranes via their lipid composition, in addition to the sensing of membranes via protein receptors. Fusion proteins create their unique lipid fingerprint that may promote the formation of fusion intermediates. These observations add to our understanding of functional roles of lipids during infection, signaling, and transport reported in earlier studies (*45, 52–57*). Given that viruses reprogram lipid synthesis during entry and assembly (*33, 58*), it becomes increasingly evident that virus–lipid interactions are important for viral replication.

Methods

Coarse-grained simulations and analysis

The lipid environment of viral fusion proteins and the binding free energies of viral protein-membrane interactions were studied using coarse-grained (CG) MD simulations. The membranes were composed of lipids mimicking the plasma membrane composition and, to better estimate the contribution of individual lipid species to binding energies, we furthermore performed simulations with membranes composed of two or three lipid types. Tables S1–S3 list the simulated membrane compositions with varying headgroup type, tail length, degree of acyl tail unsaturation. As for the structure of post-fusion viral proteins,

class I was represented using influenza A virus hemagglutinin (HA2) (Protein Data Bank ID: 1QU1) (*12*) with the fusion peptide modelled by an NMR structure (PDB ID: 1IBN) (*59*). For class II, we used the crystal structure of Rift Valley fever virus Gc (Protein Data Bank ID: 6EGU) (*13*) in wild-type form. For mutation studies, the D961K mutant was modeled using CHIMERA (*60*). For class III, the crystal structure of pseudorabies virus gB (PDB ID: 6ESC) (*15*) was used. Missing loops were modeled using MODELLER (*61*). The MARTINI 3(beta) force field was used to describe the CG systems (*62*). To set up the CG simulation systems, the atomistic protein structures were converted to CG models using the martinize script (*63*), while the secondary and tertiary structure were conserved using elastic networks. The protein–membrane systems were prepared using the insane.py script with the protein positioned slightly above the membrane surface. The system was solvated with non-polarizable MARTINI CG water and neutralized with NaCl beads. The initial configuration was energy minimized using the steepest-descent algorithm to remove bead clashes. During equilibration, a cut-off of 1.1 nm was used for Lennard-Jones and Coulombic interactions. Bond lengths were constrained using the LINCS algorithm (*64*). The temperature of 310 K was controlled using velocity rescaling with a coupling constant of 1.0 ps and the pressure of 1 bar was controlled with the semiisotropic Parrinello-Rahman (*65, 66*) barostat with a coupling contant of 12 ps. All simulations were carried out with a time step of 20 fs using GROMACS version 2020.2 (*67*).

The protein–membrane systems listed in Table S1 and S2 were simulated in triplicates, with a total simulation time of 45 μs per membrane composition. For analysis, last 10 μs of each repeat was concatenated to yield a trajectory of 30 μs per membrane composition. The lipid enrichment maps shown in Fig. 2B and Fig. S2–S5 were obtained by first computing the lipid density using gromacs tool gmx densmap, and then converted to enrichment level as described by Corradi et al. (*52*). Similarly, the lipid enrichment

index shown in Fig. 2C was also determined as described by Corradi et al. (*52*). Briefly, we compare the lipid concentration within 0.65 nm from the protein c_{prot} with the lipid concentration in the bulk membrane c_{bulk}. The enrichment index is defined as $c_{\mathrm{prot}}/c_{\mathrm{bulk}}$. Here, the gromacs tool gmx select was used to obtain the lipid concentration within 0.65 nm from the protein. In these analysis, lipid phosphate group (PO4 bead) for PC, PE, PS and SM lipids; the hydroxyl group (ROH bead) for cholesterol and AM1 bead for ganglioside GM3 were chosen as reference. For the computation of contact maps, a contact was recorded if the distance between cholesterol and protein residues was within 0.65 nm. Multiple sequence alignment and sequence identity matrices were generated using Clustal Omega (*68*). All images and plots were generated using VMD (*69*) and matplotlib (*70*).

Calculation of binding free energies

The free energy of binding was obtained from potentials of mean force (PMF) computed with umbrella sampling (US) simulations. The last frame (protein bound to membrane state) from conventional equilibration simulation served as starting structure for US simulations. The reaction coordinate was defined as the distance between the center of mass (COM) distance along z-direction (membrane normal) between the protein and the phosphate (PO4) beads of the upper, protein-bound membrane leaflet. Here only PO4 beads within the cylinder were used to compute the membrane COM, where the cylinder was aligned along the z-axis with the axis at the protein COM. The pull-cylinder-r parameter was set to 2.5 nm. This modification of the reaction coordinate avoids that the PMF is smeared out due to membrane bending. Steered MD simulations to generate frames for US simulations were performed in two stages. First, the protein was further pulled into the membrane by 0.5 nm over 50 ns with a force constant of $k = 4000\,\mathrm{kJ\,mol^{-1}\,nm^{-2}}$ and a pull rate of $1 \cdot 10^{-5}\,\mathrm{nm\,ps^{-1}}$. Next, the protein was pulled away from the membrane

surface by 3.5 nm to 4.5 nm over 240 ns, depending on the protein class and lipid composition, with a force constant of $k = 1000\,\mathrm{kJ\,mol^{-1}\,nm^{-2}}$ and a pull rate of $1.5 \cdot 10^{-5}\,\mathrm{nm\,ps^{-1}}$. Starting frames for US were taken from the steered MD simulations, with neighboring US windows spaced at 0.05 nm when protein was interacting with the membrane and 0.1 nm when protein was in the bulk water. Each window was simulated for 500 ns, while the last 400 ns were used to calculate the PMFs using the weighted histogram analysis method (*71*), as implemented by the gmx wham code (*72*). Statistical errors were estimated using 50 rounds of Bayesian bootstrapping of complete histograms (*72*). The free energy of the unbound state (at large protein–membrane distance) was defined to zero. Hence, the binding free energies ΔG_{bind} were taken from the free energy minimum of the PMFs.

Atomistic simulations

We performed extensive atomistic simulations at the microsecond time scale to (i) analyze atomic details of lipid–protein interactions and (ii) to validate that lipid binding sites are not artifacts from the simplified CG force field. From CG simulations, we selected systems with varying lipid head groups (PC, PS, PE and GM3) and lipid tail unsaturation levels, namely POPC (16:0/18:1), PLPC (16:0/18:2) and PAPC (16:0/20:4), for backmapping to all-atom resolution. The resolution transformation from CG to all-atom was carried out using the Backward tool (*73*). Next, protein crystal structures were superposed on to the structure obtained from Backward. The proteins were glycosylated using the core mannose sugars ($\mathrm{GlcNAc_2Man_3}$) using doGlycans (*74*) and later processed with the CHARMM-GUI Glycan Reader & Modeler tool (*75*). Table S4A lists the CG systems backmapped to all-atom along with the membrane composition and glycosylation sites. The glycosylated protein-membrane systems were solvated with TIP3P water (*76*) and neutralized

with NaCl ions. Additional 150mM NaCl were added to mimic the physiological salt concentration. The systems was energy minimized using the steepest-descent algorithm, followed by several rounds of short equilibration with protein backbone restrained. The CHARMM36m force field was applied for protein and lipids (*77, 78*), using corrections for cation-pi interactions by Khan et al. (*79*). Lennard-Jones forces were gradually switched off between distances of 1 nm and 1.2 nm. Coulombic interactions were treated with the particle-mesh Ewald method (*80, 81*) with a real-space cutoff at 1.2 nm. Bonds involving hydrogen atoms were constrained with LINCS (*64*). The geometry of water molecules was constrained with SETTLE (*82*). The temperature of 310 K was controlled using velocity rescaling (*83*) with a coupling constant of 1.0 ps. The pressure of 1 bar was controlled with the semiisotropic Parrinello-Rahman barostat (*65, 66*) with a coupling constant of 5 ps. The final production run was performed without restraints. Each simulation was run for 2 μs with a time step of 2 fs using GROMACS version 2020.2 (*67*). Molecular images were rendered using VMD (*69*).

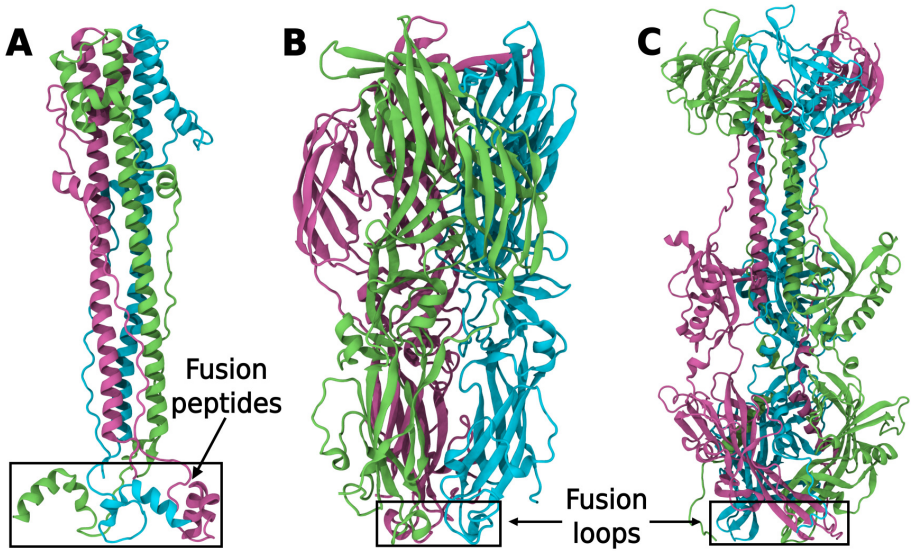

Figure 1: Post-fusion trimer structures of class I, II and III viral fusion proteins. Structures of (**A**) influenza hemagglutinin (IAV HA2; PDB IDs: 1QU1, 1IBN) (**B**) Rift Valley fever virus Gc protein (PDB ID: 6EGU), and (**C**) pseudorabies virus gB protein (PDB ID: 6ESC) are shown in cartoon representation. The monomers in each protein are colored green, pink and cyan, respectively. Black boxes highlight fusion peptide/loop regions required for binding to the host membrane.

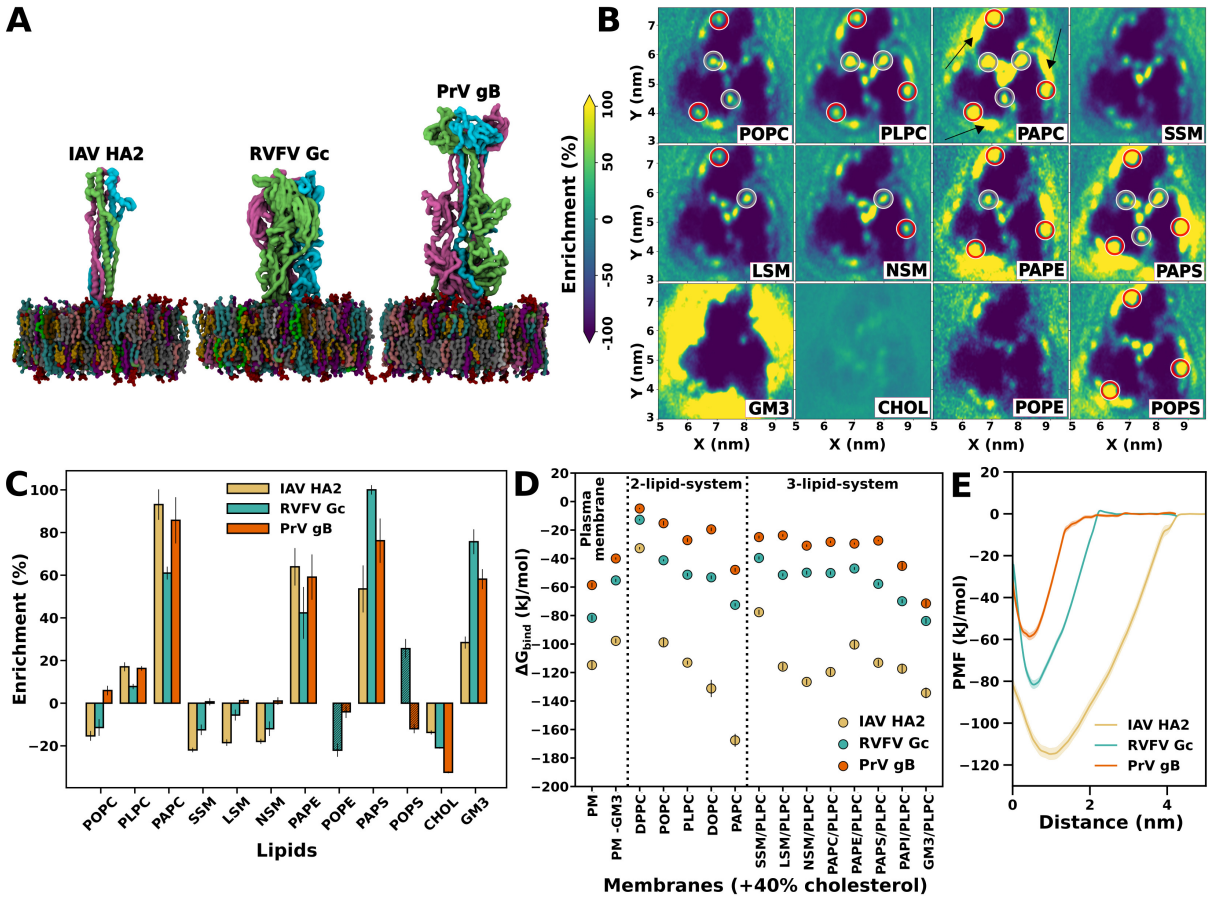

Figure 2: MD simulations of viral fusion proteins bound to lipid membranes. (**A**) Coarse-grained models of the protein–membrane complexes for IAV HA2 (left), RVFV Gc (middle), and PrV gB (right). (**B**) Two-dimensional lipid density maps for the RVFV Gc bound to the outer leaflet of a plasma membrane model. Lipid types are indicated by labels. Lipid binding sites are marked in red circles (experimental binding site) and gray circles (second binding site). Density maps for PrV gB and IAV HA2 are shown in the Figs. S2 and S3. (**C**) Enrichment of lipids of the plasma membrane in contact with the fusion protein relative to the bulk membrane. For comparison, data for POPE and POPS lipids (shaded boxes) are included from a second set of plasma membrane simulations, where PAPE and PAPS lipids were replaced by POPE and POPS lipids. Lipid enrichment map for plasma membrane containing POPE and POPS lipids are shown in the Figs. S4 and S5. (**D**) Binding free energies ΔG_{bind} taken from the free energy minimum of potentials of mean force (PMFs) of fusion protein binding, shown for IAV HA2 (brown), RVFV Gc (blue), and PrV gB (red) binding to membranes with 15 different lipid compositions. Left panel: plasma membrane (PM) and for PM depleted by GM3. Middle panel: binary mixtures of 40% cholesterol plus one phospholipid (see labels). Right panel: ternary mixtures of 40% cholesterol, 55% PLPC plus 5% of an additional lipid (see labels). (**E**) Example PMFs for fusion protein binding, here for binding to the plasma membrane model. The minima and flat regions correspond to the membrane-bound and membrane-unbound states, respectively. Vertical black bars in (C, D) and shaded areas in (E) denote 1 SE.

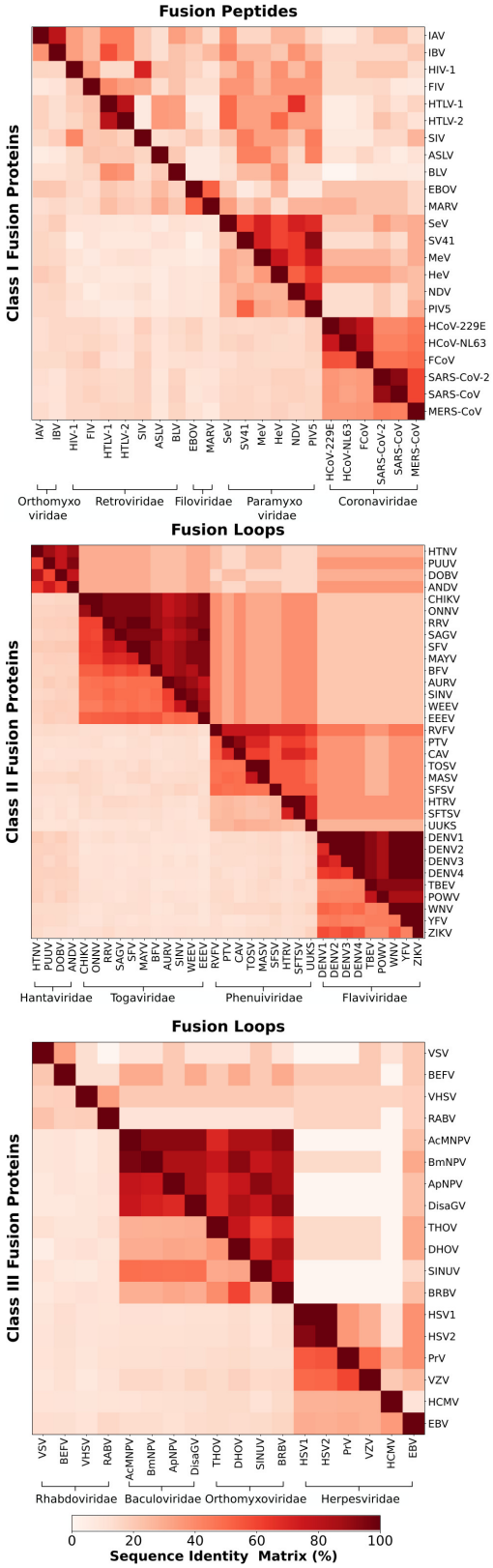

Figure 3: Sequence identity matrices of viral fusion proteins. Lower triangle shows sequence identity for fusion proteins, whereas, upper triangle shows sequence identity for fusion peptide/loops only. Sequence identities are shown for class I (upper), class II (middle), and class III proteins (lower panel). See Table S5 – S7 for the full name of viruses, fusion proteins, fusion peptide/loop sequences and UniProtKB (*84*) accession number.

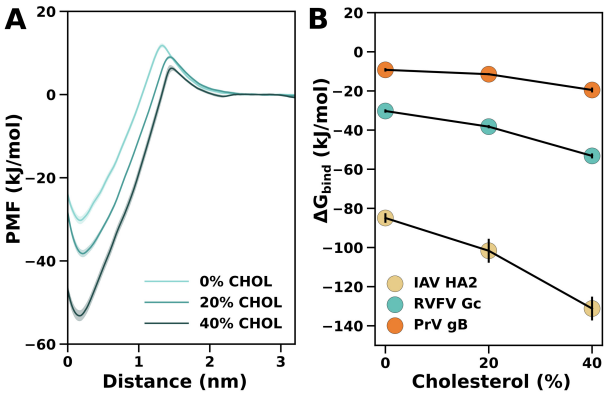

Figure 4: Cholesterol-dependent membrane binding of viral fusion proteins. (**A**) Potentials of mean force (PMFs) for RVFV Gc binding to membranes of DOPC plus 0%, 20%, or 40% cholesterol. (**B**) Binding free energies ΔG_{bind} taken from PMF calculations for three fusion proteins (see legend) with varying cholesterol concentrations. Shaded areas in (A) and vertical black bars in (B) denote 1 SE.

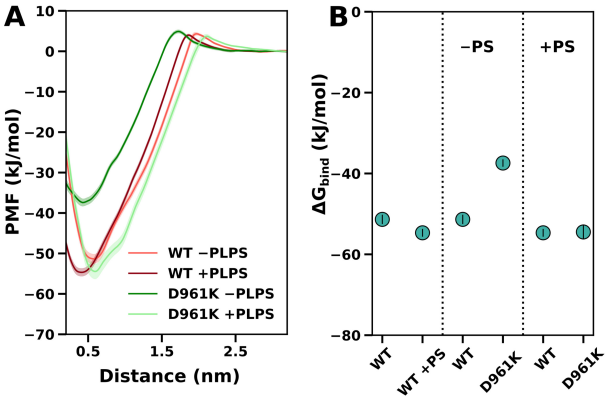

Figure 5: Effect of the D961K mutation on RVFV Gc binding to membranes. (**A**) Potentials of mean force (PMFs) for wild type (WT) and D961K mutant of RVFV Gc binding to PLPC/cholesterol/(+/− PLPS) membranes. (**B**) Binding free energies taken from the PMFs for WT and D961K RVFV Gc binding to PLPC/cholesterol/(+/− PLPS) membranes. Shaded areas in (A) and vertical black bars indicate 1 SE.

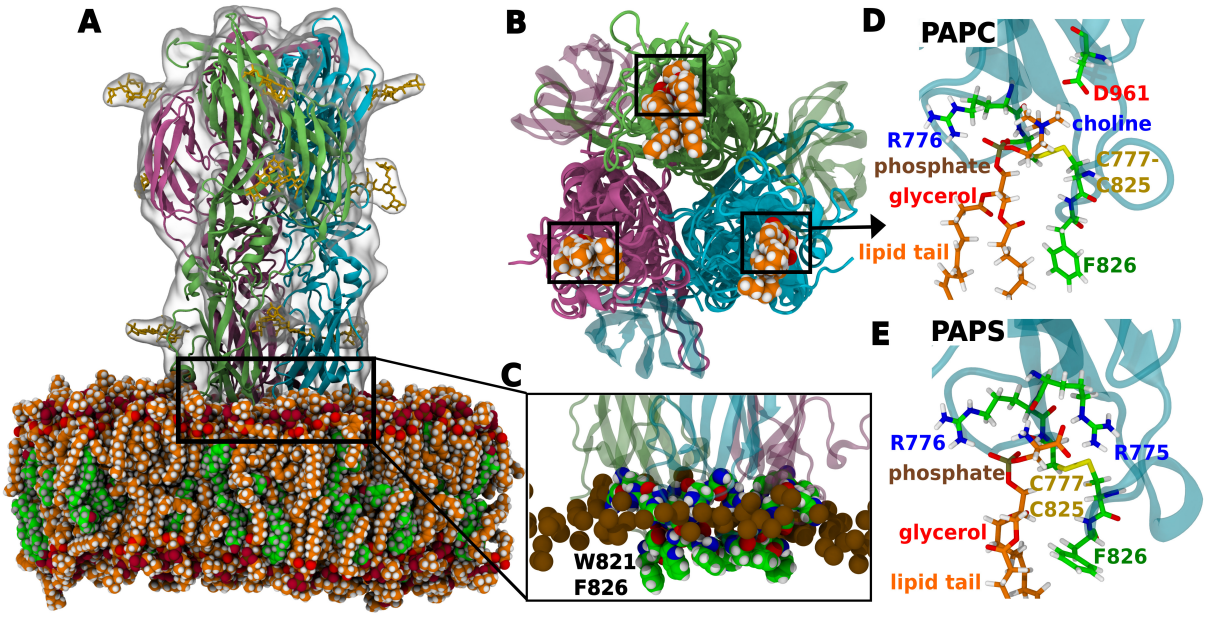

Figure 6: Lipid binding site in RVFV Gc. (**A**) All-atom simulation system of RVFV Gc in contact with a membrane of PAPC (orange/red spheres) and cholesterol (green/red spheres). Gc monomers are shown in green, pink, and cyan cartoon representation, respectively. N-Glycans on the protein are rendered as yellow sticks. Water is not shown for clarity. (**B**) Bottom view showing protein-bound PAPC rendered as orange spheres (indicated in the black box) on each monomer. (**C**) Magnified view showing interaction of fusion loops with the membrane. Fusion loop tip residues W821 and F826 from each monomer insert deep into the apolar region of the membrane below the phosphate atoms (brown spheres), whereas the rim residues R775, R776, H778, H784, N827, and N829 (colored spheres) insert into the interfacial polar region of the membrane. (**D, E**) PAPC and PAPS lipids in the same promiscuous Gc binding pocket, illustrating interactions with nearby amino acids, respectively. Choline, phosphate, glycerol and lipid tails are labeled. Lipid tails are shortened for clarity.

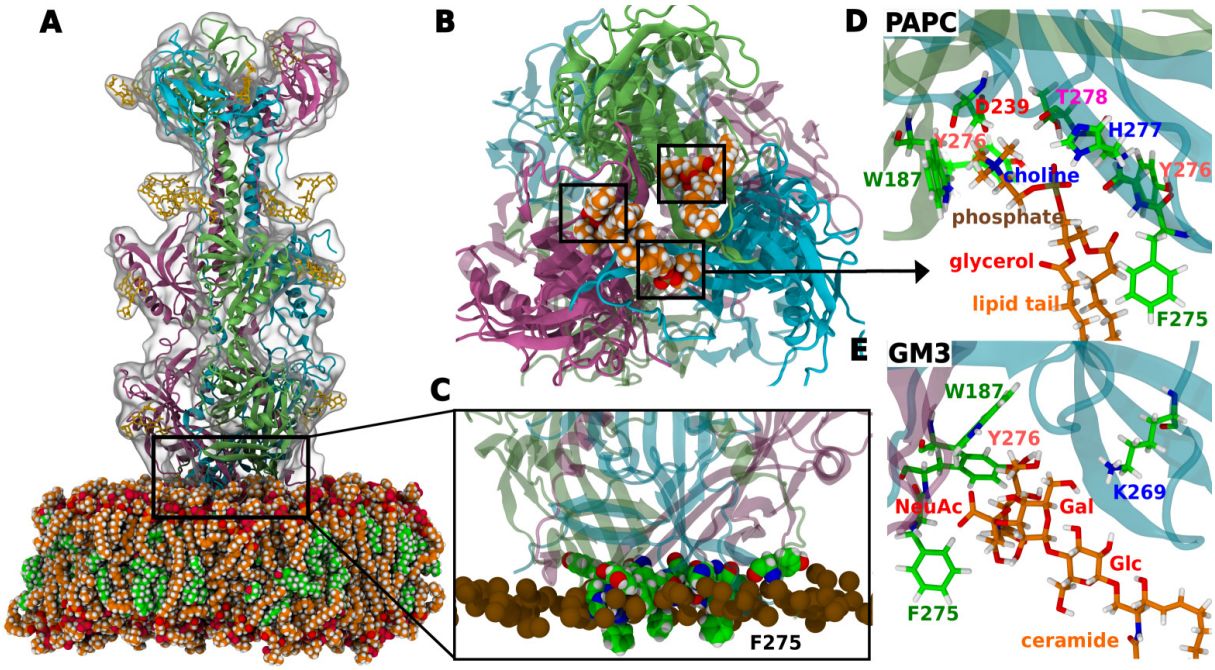

Figure 7: Lipid binding site in PrV gB. (**A**) All-atom simulation system of PrV gB in contact with a PAPC/cholesterol membrane. (**B**) Bottom view of protein-bound PAPC lipids. (**C**) Magnified view showing interactions of fusion loops with the membrane. Fusion loop tip residue F275 from each monomer inserts into the apolar region of the membrane below the phosphate atoms, whereas the rim residues Y192, W187, Y276 insert into the interfacial polar region of the membrane. (**D, E**) PAPC and GM3 lipid binding sites and their interactions with nearby amino acids, respectively. Choline, phosphate and glycerol groups are labeled for PAPC and headgroup sugars N-acetylneuraminic acid (NeuAc), galactose (Gal) and glucose (Glc) are labeled for GM3. Lipid tails are shortened for clarity. All representations and colors are chosen as in Fig. 6.

References

1. F. A. Rey, S.-M. Lok, Common Features of Enveloped Viruses and Implications for Immunogen Design for Next-Generation Vaccines. *Cell* **172**, 1319–1334 (2018).

2. M. Kielian, Mechanisms of Virus Membrane Fusion Proteins. *Annu. Rev. Virol.* (2014).

3. J. M. White, G. R. Whittaker, Fusion of enveloped viruses in endosomes. *Traffic* **17**, 593–614 (2016).

4. M. Kielian, F. A. Rey, Virus membrane-fusion proteins: more than one way to make a hairpin. *Nat. Rev. Microbiol.* **4**, 67–76 (2006).

5. R. Jahn, T. Lang, T. C. Südhof, Membrane fusion. *Cell* **112**, 519–533 (2003).

6. W. Wickner, R. Schekman, Membrane fusion. *Nat. Struct. Mol. Biol.* **15**, 658–664 (2008).

7. Y. Kozlovsky, M. M. Kozlov, Stalk model of membrane fusion: solution of energy crisis. *Biophys. J.* **82**, 882–895 (2002).

8. S. Aeffner, T. Reusch, B. Weinhausen, T. Salditt, Energetics of stalk intermediates in membrane fusion are controlled by lipid composition. *Proc. Natl. Acad. Sci.* **109**, E1609–18 (2012).

9. L. V. Chernomordik, M. M. Kozlov, Protein-lipid interplay in fusion and fission of biological membranes. *Annu. Rev. Biochem.* **72**, 175–207 (2003).

10. L. V. Chernomordik, J. Zimmerberg, M. M. Kozlov, Membranes of the world unite! *J. Cell Biol.* **175**, 201–207 (2006).

11. S. C. Harrison, Viral membrane fusion. *Nat. Struct. Mol. Biol.* **15**, 690–698 (2008).

12. J. Chen, J. J. Skehel, D. C. Wiley, N- and C-terminal residues combine in the fusion-pH influenza hemagglutinin HA_2 subunit to form an N cap that terminates the triple-stranded coiled coil. *Proc. Natl. Acad. Sci.* **96**, 8967– 8972 (1999).

13. P. Guardado-Calvo, K. Atkovska, S. A. Jeffers, N. Grau, M. Backovic, J. Pérez-Vargas, S. M. De Boer, M. A. Tortorici, G. Pehau-Arnaudet, J. Lepault, P. England, P. J. Rottier, B. J. Bosch, J. S. Hub, F. A. Rey, A glycerophospholipid-specific pocket in the RVFV class II fusion protein drives target membrane insertion. *Science* **358**, 663–667 (2017).

14. M. Backovic, T. S. Jardetzky, Class III viral membrane fusion proteins. *Curr. Opin. Struct. Biol.* **19**, 189–196 (2009).

15. M. Vallbracht, D. Brun, M. Tassinari, M.-C. Vaney, G. Pehau-Arnaudet, P. Guardado-Calvo, A. Haouz, B. G. Klupp, T. C. Mettenleiter, F. A. Rey, M. Backovic, Structure-function dissection of pseudorabies virus glycoprotein B fusion loops. *J. Virol.* **92**, e01203–17 (2018).

16. M. Umashankar, C. Sánchez-San Martín, M. Liao, B. Reilly, A. Guo, G. Taylor, M. Kielian, Differential cholesterol binding by class II fusion proteins determines membrane fusion properties. *J. Virol.* **82**, 9245–9253 (2008).

17. M. C. Kielian, A. Helenius, Role of cholesterol in fusion of Semliki Forest virus with membranes. *J. Virol.* **52**, 281–283 (1984).

18. G. Meher, S. Sinha, G. P. Pattnaik, S. Ghosh Dastidar, H. Chakraborty, Cholesterol Modulates Membrane Properties and the Interaction of gp41 Fusion Peptide To Promote Membrane Fusion. *J. Phys. Chem. B* **123**, 7113–7122 (2019).

19. G. Meher, S. Bhattacharjya, H. Chakraborty, Membrane Cholesterol Modulates Oligomeric Status and Peptide-Membrane Interaction of Severe Acute Respiratory Syndrome Coronavirus Fusion Peptide. *J. Phys. Chem. B* **123**, 10654–10662 (2019).

20. G. A. Wudiri, S. M. Pritchard, H. Li, J. Liu, H. C. Aguilar, S. D. Gilk, A. V. Nicola, Molecular requirement for sterols in herpes simplex virus entry and infectivity. *J. Virol.* **88**, 13918–13922 (2014).

21. X. Ren, J. Yin, G. Li, G. Herrler, Cholesterol dependence of pseudorabies herpesvirus entry. *Curr. Microbiol.* **62**, 261–266 (2011).

22. A. S. Desplanques, H. J. Nauwynck, D. Vercauteren, T. Geens, H. W. Favoreel, Plasma membrane cholesterol is required for efficient pseudorabies virus entry. *Virology* **376**, 339–345 (2008).

23. D. W. Sanders, C. C. Jumper, P. J. Ackerman, D. Bracha, A. Donlic, H. Kim, D. Kenney, I. Castello-Serrano, S. Suzuki, T. Tamura, A. H. Tavares, M. Saeed, A. S. Holehouse, A. Ploss, I. Levental, F. Douam, R. F. Padera, B. D. Levy, C. P. Brangwynne, SARS-CoV-2 requires cholesterol for viral entry and pathological syncytia formation. *Elife* **10**, e65962 (2021).

24. A. Ahn, D. L. Gibbons, M. Kielian, The fusion peptide of Semliki Forest virus associates with sterol-rich membrane domains. *J. Virol.* **76**, 3267–3275 (2002).

25. I. Schuffenecker, I. Iteman, A. Michault, S. Murri, L. Frangeul, M.-C. Vaney, R. Lavenir, N. Pardigon, J.-M. Reynes, F. Pettinelli, L. Biscornet, L. Diancourt, S. Michel, S. Duquerroy, G. Guigon, M.-P. Frenkiel, A.-C. Bréhin, N. Cubito, P. Desprès, F. Kunst, F. A. Rey, H. Zeller, S. Brisse, Genome microevolution of chikungunya viruses causing the Indian Ocean outbreak. *PLoS Med.* **3**, e263 (2006).

26. S. N. Tantirimudalige, P. V. Raghuvamsi, K. K. Sharma, J. C. Wei Bao, G. S. Anand, T. Wohland, The ganglioside GM1a functions as a coreceptor/attachment factor for dengue virus during infection. *J. Biol. Chem.* **298**, 102570 (2022).

27. Y. Suzuki, M. Matsunaga, M. Matsumoto, N-Acetylneuraminyllactosylceramide, GM3-NeuAc, a new influenza A virus receptor which mediates the adsorption-fusion process of viral infection. Binding specificity of influenza virus A/Aichi/2/68 (H3N2) to membrane-associated GM3 with different molecular. *J. Biol. Chem.* **260**, 1362–1365 (1985).

28. Y. Suzuki, Gangliosides as influenza virus receptors. Variation of influenza viruses and their recognition of the receptor sialo-sugar chains. *Prog. Lipid Res.* **33**, 429–457 (1994).

29. J. H. Lorent, K. R. Levental, L. Ganesan, G. Rivera-Longsworth, E. Sezgin, M. Doktorova, E. Lyman, I. Levental, Plasma membranes are asymmetric in lipid unsaturation, packing and protein shape. *Nat. Chem. Biol.* **16**, 710 (2020).

30. R. Peng, S. Zhang, Y. Cui, Y. Shi, G. F. Gao, J. Qi, Structures of human-infecting thogotovirus fusogens support a common ancestor with insect baculovirus. *Proc. Natl. Acad. Sci.* **114**, E8905-E8912 (2017).

31. X. Han, L. K. Tamm, A host–guest system to study structure–function relationships of membrane fusion peptides. *Proc. Natl. Acad. Sci.* **97**, 13097–13102 (2000).

32. M. Pinot, S. Vanni, S. Pagnotta, S. Lacas-Gervais, L.-A. Payet, T. Ferreira, R. Gautier, B. Goud, B. Antonny, H. Barelli, Lipid cell biology. Polyunsaturated phospholipids facilitate membrane deformation and fission by endocytic proteins. *Science* **345**, 693–697 (2014).

33. S. E. Farley, J. E. Kyle, H. C. Leier, L. M. Bramer, J. B. Weinstein, T. A. Bates, J. Y. Lee, T. O. Metz, C. Schultz, F. G. Tafesse, A global lipid map reveals host dependency factors conserved across sars-cov-2 variants. *Nat. Commun.* **13**, 1-14 (2022).

34. T. Maeda, K. Kawasaki, S. Ohnishi, Interaction of influenza virus hemagglutinin with target membrane lipids is a key step in virus-induced hemolysis and fusion at pH 5.2. *Proc. Natl. Acad. Sci.* **78**, 4133–4137 (1981).

35. J. L. Miller, D. J. Weed, B. H. Lee, S. M. Pritchard, A. V. Nicola, Low-ph endocytic entry of the porcine alphaherpesvirus pseudorabies virus. *J. Virol.* **93** (2019).

36. K. A. Connors, A. L. Hartman, Advances in understanding neuropathogenesis of rift valley fever virus. *Annu. Rev. Virol.* **9**, 437–450 (2022).

37. M. Luo, Influenza virus entry. *Adv. Exp. Med. Biol.* **726**, 201–221 (2012).

38. T. Kobayashi, M. H. Beuchat, J. Chevallier, A. Makino, N. Mayran, J. M. Escola, C. Lebrand, P. Cosson, T. Kobayashi, J. Gruenberg, Separation and characterization of late endosomal membrane domains. *J. Biol. Chem.* **277**, 32157–32164 (2002).

39. G. V. Meer, D. R. Voelker, G. W. Feigenson, Membrane lipids: where they are and how they behave. *Nat. Rev. Mol. Cell Biol.* **9**, 112–124 (2008).

40. S. Arumugam, A. Kaur, The lipids of the early endosomes: Making multimodality work. *ChemBioChem* **18**, 1053–1060 (2017).

41. E. Zaitseva, S. T. Yang, K. Melikov, S. Pourmal, L. V. Chernomordik, Dengue virus ensures its fusion in late endosomes using compartment-specific lipids. *PLoS Pathog.* **6**, e1001131 (2010).

42. P. M. Matos, M. Marin, B. Ahn, W. Lam, N. C. Santos, G. B. Melikyan, Anionic lipids are required for vesicular stomatitis virus g protein-mediated single particle fusion with supported lipid bilayers. *J. Biol. Chem.* **288**, 12416–12425 (2013).

43. A. B. García-Arribas, E. J. González-Ramírez, J. Sot, I. Areso, A. Alonso, F. M. Goñi, Complex Effects of 24:1 Sphingolipids in Membranes Containing Dioleoylphosphatidylcholine and Cholesterol. *Langmuir* **33**, 5545–5554 (2017).

44. E. J. González-Ramírez, A. B. García-Arribas, J. Sot, F. M. Goñi, A. Alonso, C24:0 and C24:1 sphingolipids in cholesterol-containing, five- and six-component lipid membranes. *Sci. Rep.* **10**, 14085 (2020).

45. C. Favard, J. Chojnacki, P. Merida, N. Yandrapalli, J. Mak, C. Eggeling, D. Muriaux, HIV-1 Gag specifically restricts PI(4,5)P2 and cholesterol mobility in living cells creating a nanodomain platform for virus assembly. *Sci. Adv.* **5**, eaaw8651 (2019).

46. T. Ivanovic, J. L. Choi, S. P. Whelan, A. M. van Oijen, S. C. Harrison, Influenza-virus membrane fusion by cooperative fold-back of stochastically induced hemagglutinin intermediates. *Elife* **2013**, e00333 (2013).

47. T. Danieli, S. L. Pelletier, Y. I. Henis, J. M. White, Membrane fusion mediated by the influenza virus hemagglutinin requires the concerted action of at least three hemagglutinin trimers. *J. Cell Biol.* **133**, 559–569 (1996).

48. D. L. Floyd, J. R. Ragains, J. J. Skehel, S. C. Harrison, A. M. van Oijen, Single-particle kinetics of influenza virus membrane fusion. *Proc. Natl. Acad. Sci.* **105**, 15382–15387 (2008).

49. C. S. Poojari, K. C. Scherer, J. S. Hub, Free energies of membrane stalk formation from a lipidomics perspective. *Nat. Commun.* **12**, 6594 (2021).

50. K. M. Gallegos, D. G. Conrady, S. S. Karve, T. S. Gunasekera, A. B. Herr, A. A. Weiss, Shiga toxin binding to glycolipids and glycans. *PLoS One* **7**, e30368–e30368 (2012).

51. G. M. Kuziemko, M. Stroh, R. C. Stevens, Cholera Toxin Binding Affinity and Specificity for Gangliosides Determined by Surface Plasmon Resonance. *Biochemistry* **35**, 6375–6384 (1996).

52. V. Corradi, E. Mendez-Villuendas, H. I. Ingólfsson, R.-X. Gu, I. Siuda, M. N. Melo, A. Moussatova, L. J. DeGagné, B. I. Sejdiu, G. Singh, T. A. Wassenaar, K. Delgado Magnero, S. J. Marrink, D. P. Tieleman, LipidProtein Interactions Are Unique Fingerprints for Membrane Proteins. *ACS Cent. Sci.* **4**, 709–717 (2018).

53. J. Shearer, D. Jefferies, S. Khalid, Outer Membrane Proteins OmpA, FhuA, OmpF, EstA, BtuB, and OmpX Have Unique Lipopolysaccharide Fingerprints. *J. Chem. Theory Comput.* **15**, 2608–2619 (2019).

54. K. I. P. Le Huray, H. Wang, F. Sobott, A. C. Kalli, Systematic simulation of the interactions of pleckstrin homology domains with membranes. *Sci. Adv.* **8**, eabn6992 (2022).

55. S. Chatterjee, D. Maltseva, Y. Kan, E. Hosseini, G. Gonella, M. Bonn, S. H. Parekh, Lipid-driven condensation and interfacial ordering of FUS. *Sci. Adv.* **8**, eabm7528 (2022).

56. E. Yamamoto, J. Domański, F. B. Naughton, R. B. Best, A. C. Kalli, P. J. Stansfeld, M. S. P. Sansom, Multiple lipid binding sites determine the affinity of PH domains for phosphoinositide-containing membranes. *Sci. Adv.* **6**, eaay5736 (2020).

57. A. L. Duncan, R. A. Corey, M. S. P. Sansom, Defining how multiple lipid species interact with inward rectifier potassium (Kir2) channels. *Proc. Natl. Acad. Sci.* **117**, 7803–7813 (2020).

58. M. Mazzon, J. Mercer, Lipid interactions during virus entry and infection. *Cell. Microbiol.* **16**, 1493–1502 (2014).

59. X. Han, J. H. Bushweller, D. S. Cafiso, L. K. Tamm, Membrane structure and fusion-triggering conformational change of the fusion domain from influenza hemagglutinin. *Nat. Struct. Biol.* **8**, 715–720 (2001).

60. E. F. Pettersen, T. D. Goddard, C. C. Huang, G. S. Couch, D. M. Greenblatt, E. C. Meng, T. E. Ferrin, UCSF Chimera - A visualization system for exploratory research and analysis. *J Comput Chem.* **25**, 1605–1612 (2004).

61. N. Eswar, B. Webb, M. A. Marti-Renom, M. S. Madhusudhan, D. Eramian, M.-y. Shen, U. Pieper, A. Sali, Comparative protein structure modeling using Modeller. *Curr. Protoc. Bioinforma.* p. chapter 2 (2007).

62. P. C. Souza, R. Alessandri, J. Barnoud, S. Thallmair, I. Faustino, F. Grnewald, I. Patmanidis, H. Abdizadeh, B. M. Bruininks, T. A. Wassenaar, P. C. Kroon, J. Melcr, V. Nieto, V. Corradi, H. M. Khan, J. Domaski, M. Javanainen, H. Martinez-Seara, N. Reuter, R. B. Best, I. Vattulainen, L. Monticelli, X. Periole, D. P. Tieleman, A. H. de Vries, S. J. Marrink, Martini 3: a general purpose force field for coarse-grained molecular dynamics. *Nat. Methods* **18**, 382-388 (2021).

63. D. H. de Jong, G. Singh, W. F. D. Bennett, C. Arnarez, T. A. Wassenaar, L. V. Schäfer, X. Periole, D. P. Tieleman, S. J. Marrink, Improved Parameters for the

Martini Coarse-Grained Protein Force Field. *J. Chem. Theory Comput.* **9**, 687–697 (2013).

64. B. Hess, H. Bekker, H. J. C. Berendsen, J. G. E. M. Fraaije, LINCS: A linear constraint solver for molecular simulations. *J. Comput. Chem.* **18**, 1463–1472 (1997).

65. M. Parrinello, Polymorphic transitions in single crystals: A new molecular dynamics method. *J. Appl. Phys.* **52**, 7182–7190 (1981).

66. M. Parrinello, A. Rahman, Crystal structure and pair potentials: A molecular-dynamics study. *Phys. Rev. Lett.* (1980).

67. M. J. Abraham, T. Murtola, R. Schulz, S. Páll, J. C. Smith, B. Hess, E. Lindah, Gromacs: High performance molecular simulations through multi-level parallelism from laptops to supercomputers. *SoftwareX* **1-2**, 19–25 (2015).

68. F. Sievers, A. Wilm, D. Dineen, T. J. Gibson, K. Karplus, W. Li, R. Lopez, H. McWilliam, M. Remmert, J. Sding, J. D. Thompson, D. G. Higgins, Fast, scalable generation of high-quality protein multiple sequence alignments using clustal omega. *Mol. Syst. Biol.* **7**, 539 (2011).

69. W. Humphrey, A. Dalke, K. Schulten, VMD: Visual molecular dynamics. *J. Mol. Graph.* **14**, 33–38 (1996).

70. J. D. Hunter, Matplotlib: A 2d graphics environment. *Comput. Sci. Eng.* **9**, 90–95 (2007).

71. S. Kumar, D. Bouzida, R. H. Swendsen, P. A. Kollman, J. M. Rosenberg, The weighted histogram analysis method for free-energy calculations on biomolecules. 1: The method. *J. Comput. Chem* **13**, 1011–1021 (1992).

72. J. S. Hub, B. L. De Groot, D. Van Der Spoel, G-whams-a free Weighted Histogram Analysis implementation including robust error and autocorrelation estimates. *J. Chem. Theory Comput.* **6 (12)**, 3713–3720 (2010).

73. T. A. Wassenaar, K. Pluhackova, R. A. Böckmann, S. J. Marrink, D. P. Tieleman, Going Backward: A Flexible Geometric Approach to Reverse Transformation from Coarse Grained to Atomistic Models. *J. Chem. Theory Comput.* **10**, 676–690 (2014).

74. R. Danne, C. Poojari, H. Martinez-Seara, S. Rissanen, F. Lolicato, T. Róg, I. Vattulainen, DoGlycans-Tools for Preparing Carbohydrate Structures for Atomistic Simulations of Glycoproteins, Glycolipids, and Carbohydrate Polymers for GROMACS. *J. Chem. Inf. Model.* **57**, 2401–2406 (2017).

75. S.-J. Park, J. Lee, Y. Qi, N. R. Kern, H. S. Lee, S. Jo, I. Joung, K. Joo, J. Lee, W. Im, CHARMM-GUI Glycan Modeler for modeling and simulation of carbohydrates and glycoconjugates. *Glycobiology* **29**, 320–331 (2019).

76. W. L. Jorgensen, J. Chandrasekhar, J. D. Madura, R. W. Impey, M. L. Klein, Comparison of simple potential functions for simulating liquid water. *J. Chem. Phys.* **79**, 926–935 (1983).

77. J. Huang, S. Rauscher, G. Nawrocki, T. Ran, M. Feig, B. L. de Groot, H. Grubmüller, A. D. MacKerell, CHARMM36m: an improved force field for folded and intrinsically disordered proteins. *Nat. Methods* **14**, 71–73 (2017).

78. R. W. Pastor, A. D. MacKerell, Development of the charmm force field for lipids. *J. Phys. Chem. Lett.* **2**, 1526-1532 (2011).

79. H. M. Khan, A. D. MacKerell, N. Reuter, Cation-π Interactions between Methylated Ammonium Groups and Tryptophan in the CHARMM36 Additive Force Field. *J. Chem. Theory Comput.* **15**, 7–12 (2019).

80. T. Darden, D. York, L. Pedersen, Particle mesh ewald: An nlog(n) method for ewald sums in large systems. *J. Chem. Phys.* **98**, 10089 (1998).

81. U. Essmann, L. Perera, M. L. Berkowitz, T. Darden, H. Lee, L. G. Pedersen, A smooth particle mesh ewald method. *J. Chem. Phys.* **103**, 8577 (1998).

82. S. Miyamoto, P. A. Kollman, Settle: An analytical version of the shake and rattle algorithm for rigid water models. *J. Comput. Chem.* **13**, 952-962 (1992).

83. G. Bussi, D. Donadio, M. Parrinello, Canonical sampling through velocity rescaling. *J. Chem. Phys.* **126**, 014101–7 (2007).

84. A. Bateman, *et al.*, Uniprot: the universal protein knowledgebase. *Nucleic Acids Res.* **45**, D158-D169 (2017).

Acknowledgments

We thank Marija Backovic for critical reading of this manuscript. **Funding:** This study was supported by the Deutsche Forschungsgemeinschaft via SFB 1027/B7. **Author contributions:** Conceptualization: CSP, JSH. Methodology: CSP, JSH. Investigation: CSP, TB. Visualization: CSP, TB. Supervision: JSH. Writingoriginal draft: CSP. Writingreview & editing: CSP, JSH. **Competing interests:** Authors declare that they have no competing interests. **Data and materials availability:** All data are available in the main text and/or the supplementary materials. Coarse-grained and all-atom structure

files, topologies, parameter files, backmapping files, and other related files required to reproduce the simulation data are available at Zenodo: https://doi.org/10.5281/zenodo.7945458.

Supplementary materials

The Supplementary PDF includes:
Figs. S1 to S9
Tables S1 to S7
Supplementary Text
Supplementary References